



HAL
open science

Determination of mass transfer coefficient in flow assisted corrosion of steel in liquid Pb Bi. Rotating cylinder geometry

L. Martinelli, F. Balbaud-Célérier, C. Alémany-Dumont, Valéry Botton

► To cite this version:

L. Martinelli, F. Balbaud-Célérier, C. Alémany-Dumont, Valéry Botton. Determination of mass transfer coefficient in flow assisted corrosion of steel in liquid Pb Bi. Rotating cylinder geometry. International Communications in Heat and Mass Transfer, 2022, 133, pp.105960. 10.1016/j.icheatmasstransfer.2022.105960 . hal-03603535

HAL Id: hal-03603535

<https://hal.science/hal-03603535>

Submitted on 9 Mar 2022

HAL is a multi-disciplinary open access archive for the deposit and dissemination of scientific research documents, whether they are published or not. The documents may come from teaching and research institutions in France or abroad, or from public or private research centers.

L'archive ouverte pluridisciplinaire **HAL**, est destinée au dépôt et à la diffusion de documents scientifiques de niveau recherche, publiés ou non, émanant des établissements d'enseignement et de recherche français ou étrangers, des laboratoires publics ou privés.

Determination of mass transfer coefficient in flow assisted corrosion of steel in liquid Pb-Bi. Rotating cylinder geometry.

L. Martinelli^a, F. Balbaud-Célérier^a, C. Alémany-Dumont^b, V. Botton^{c*}

^a *Université Paris-Saclay, CEA, Service de la Corrosion et du Comportement des Matériaux dans leur Environnement, 91191, Gif-sur-Yvette, France*

^b *Univ Lyon, INSA Lyon, UMR CNRS 5510, Laboratoire MATEIS, F-69621 Villeurbanne Cedex, France*

^c *Univ Lyon, INSA Lyon, CNRS, Ecole Centrale de Lyon, Univ Claude Bernard Lyon 1, LMFA, UMR5509, 69621, Villeurbanne France.*

*: *corresponding author*
tel: +33 4 72 43 70 19
e-mail address: valery.botton@insa-lyon.fr

Abstract:

The aim of this experimental and numerical work is to determine the mass transfer at the wall of a steel cylinder rotating within liquid Lead-Bismuth blend. This is a crucial parameter for the analysis of corrosion tests performed in the CICLAD experimental set-up for the investigation of flow assisted corrosion of steel by liquid metals. As a reliable numerical modelling must rely on experimental validation, and since no direct wall mass transfer measurement is possible in CICLAD, a scaled electrochemical model has been achieved. Modelling the turbulence in this rotating configuration is shown to require the use of a Reynolds-Stress Model. A sensitivity to the Schmidt number is observed in the numerical simulations representing the measured mass transfer in the electrochemical model. Simulations dedicated to liquid Pb-Bi are thus presented in addition to those dedicated to the aqueous solution used in the electrochemical model. Following correlations are proposed for the prediction of Fe mass transfer at the wall of a steel rotating cylinder in liquid Pb-Bi:

$$Sh=1.9 \times 10^{-1} (Re^2 Sc)^{0.31} \text{ for } 2 \times 10^9 < Re^2 Sc < 5.3 \times 10^{10};$$

$$Sh=1.4 \times 10^{-3} (Re^2 Sc)^{0.51} \text{ for } 5.3 \times 10^{10} < Re^2 Sc < 8.5 \times 10^{11};$$

$$Sh=1.1 \times 10^{-2} (Re^2 Sc)^{0.43} \text{ for } 8.5 \times 10^{11} < Re^2 Sc < 10^{13}.$$

This mass transfer coefficient has recently been used to get a better understanding of corrosion in Pb-Bi [1].

Highlights :

- Mass transfer coefficient for steel in liquid LBE are measured in a rotating cylinder configuration in the CICLAD set-up,
- The hydrodynamics of CICLAD is modelled both numerically and experimentally,
- A scaled electrochemical model experiment in similarity with CICLAD is used to validate the numerical model.
- Correlations are proposed depending on the Schmidt and Reynolds numbers.

Key words:

Mass transfer measurements, dissolution, corrosion, liquid metal, hydrodynamics, rotating cylinder, correlations.

Introduction

Lead alloys, and particularly lead-bismuth eutectic (LBE), are considered as primary coolant in Pb-Bi cooled fast reactors and in Accelerator Driven Systems. However, lead alloys can be corrosive toward steels and particularly towards Fe-9Cr steels [2–16]. Steel corrosion process depends mainly on the concentration of dissolved oxygen in Pb-Bi and the velocity of the liquid alloy. Indeed, for oxygen concentrations lower than the one necessary for magnetite formation (approximately 10^{-8} wt % at temperature around 500°C for Fe-9Cr steels), the corrosion process is steel dissolution [1,17,18]. Then, in the case of a dissolution process, one essential parameter influencing the corrosion process and thus the corrosion rate is the fluid flow intensity.

Three domains can be observed [1,17,18]. For low fluid velocity, the steel corrosion rate increases when fluid velocity increases, it is mass transfer controlled. When fluid velocity reaches a threshold value, the corrosion rate becomes independent of the fluid velocity and the corrosion rate is in the domain of activation (*i.e.* dissolution reaction rate) control until the fluid velocity becomes sufficiently high to erode steel [19] – which is the erosion-corrosion domain.

Considering a duct flow configuration, Balbaud *et al* [17] have shown that experimental corrosion rate of Fe-9Cr steel and pure Fe increased for increasing liquid Pb-Bi eutectic velocity. They concluded that in the considered range of parameters, fluid velocity controlled the corrosion rate and that the hydrodynamic effect on corrosion has to be carefully studied. In order to study this effect, the hydrodynamics has to be well characterized in the working system geometry. They have thus designed an experimental set-up dedicated to the investigation of flow assisted corrosion of steels by Pb-Bi, namely the CICLAD set-up [17].

In cooled lead-bismuth reactors, the fluid flow is turbulent. In the present study, the system geometry has consequently been chosen to ensure turbulent flow conditions in small facilities: the corrosion sample is a steel cylinder rotating in a crucible filled by liquid lead-bismuth. Expectedly, Fe corrosion rate also increases when the angular velocity of Fe cylinder increases from 0 to 525 rad s⁻¹ as seen on Figure 1 [18].

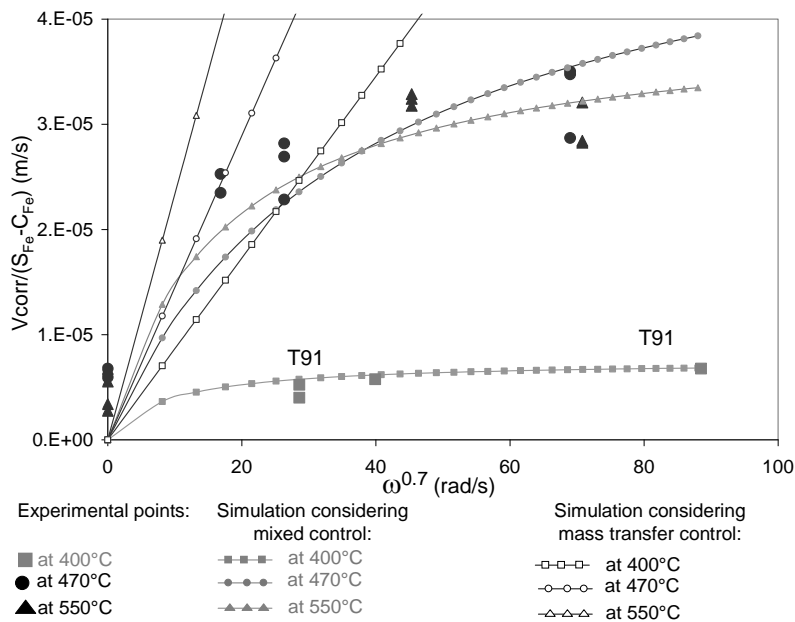


Figure 1: Ratio between the corrosion rate and difference between iron solubility limit in liquid Pb-Bi and dissolved Fe concentration in Pb-Bi bulk as a function of the angular velocity at 400°C [17], 470°C and 540°C. Experimental data and modelling.

Balbaud *et al* [17] also demonstrated in this rotating cylinder geometry, that the relevant parameter to be considered to model the fluid flow effects on corrosion is the mass transfer coefficient rather than the

flow velocity. Consequently, understanding and modeling corrosion results obtained in the CICLAD facility require the determination of the mass transfer coefficient, K , which is the aim of the present study.

Note that mass transfer coefficients for rotating cylinder configuration are given in literature by [20–22] but these are, a priori, valid for infinitely long rotating cylinder configuration. As the CICLAD facility [17] exhibits a confined geometry, the mass transfer coefficient in the CICLAD geometry has thus to be determined by other ways, such as the use of Computational Fluid Dynamics (CFD) numerical simulations. However, one must keep in mind that accounting for turbulent mass transport in confined, rotating, configurations is not so easy. The results of CFD simulations in this type of configurations are indeed expected to be sensitive to the numerical model parameters, in particular concerning the turbulence model.

As a consequence, in order to validate the computational model, the following method is developed: the mass transfer coefficient in CICLAD geometry is determined by two ways (i) by CFD simulation, using the Fluent™ software; (ii) by electrochemical experiments in aqueous electrolyte in the same geometry as CICLAD. The results obtained with the CFD model are compared to those obtained in the electrochemical experiment for a selected parameters range in order to judge the ability of the CFD model to predict the mass transfer coefficient at the rotating cylinder wall. The validated CFD model is then used to investigate a more extended parameters range. Finally, interpretation of experimental corrosion results, using this study, are presented in detail in our former paper [1].

1 List of Symbols

A : sample surface area (m^2)

a : constant

b : constant

$C_{Fe}^{LBE}(b)$: concentration of dissolved Fe in the LBE bulk (mol cm^{-3})

d : electrode or CICLAD sample diameter (cm)

D : diffusion coefficient of dissolved species in liquid Pb-Bi ($\text{cm}^2 \text{s}^{-1}$)

D_{Fe} : iron diffusion coefficient in Pb-Bi ($\text{cm}^2 \text{s}^{-1}$)

$D_{Fe^{3+}}$: ferric ion diffusion coefficient in water ($\text{cm}^2 \text{s}^{-1}$)

E : activation energy of dissolution rate constant (J mol^{-1})

F : Faraday's constant (C mol^{-1})

$[\text{Fe}^{3+}]$: ferric ions content in the solution (mol cm^{-3})

J_{stat} : steady state current (A)

K : mass transfer coefficient (cm s^{-1})

k_d : dissolution rate constant ($\text{mol cm}^{-2} \text{s}^{-1}$)

Fe_d : dissolved Fe in Pb-Bi

M_{Fe} : molar mass of Fe (g mol^{-1})

Fe_s : solid Fe

m_{Fe}^{LBE} : mass of dissolved Fe in LBE (g)

R : gas constant ($\text{J mol}^{-1} \text{K}^{-1}$)

Re : Reynolds number

S_{Fe} : solubility limit of Fe in LBE (mol cm^{-3})

Sc : Schmidt number

Sh : Sherwood number

t : time (s)

T : temperature ($^{\circ}\text{C}$ or K)

δ : diffusion boundary layer thickness (cm)

η : dynamic viscosity (Pa s)

ν : kinematic viscosity ($\text{cm}^2 \text{s}^{-1}$)

ω : angular velocity (rad s^{-1})

ρ : density (g cm^{-3})

2 CICLAD geometry and methods

2-1 CICLAD geometry and geometry of electrochemical cell

The CICLAD device is dedicated to corrosion experiments in flowing Pb-Bi; it is a corrosion loop schematically represented in Figure 2. In this facility, dissolution experiments are performed in liquid lead-bismuth eutectic (LBE) containing in wt%: 44.8% lead, 55.2% bismuth and in weight ppm: $[\text{Ag}] = 5$, $[\text{Fe}] < 0.2$, $[\text{Cu}] < 0.7$. As Balbaud *et al* [17] showed that corrosion rate and mechanism of Fe-9Cr steel are the

same as that of pure iron, tests are carried out using either Fe-9Cr steel or pure iron from ARMCO® between 450 and 553°C [1].

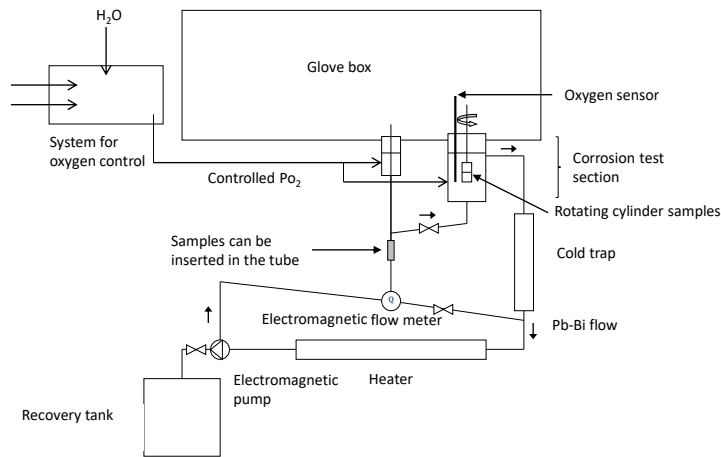


Figure 2. Sketch of CICLAD facility.

The corrosion test section consists of a tank containing 5L of LBE in a glove box. Its loop is a circuit dedicated to the continuous purification of the liquid alloy. Iron cylinders fixed along a rotating shaft as represented on Figure 3a are used as samples. Their angular velocity can be adjusted between 35 and 450 $\text{rad}\cdot\text{s}^{-1}$. Their diameter and approximate length are respectively 8 mm and 20 mm. They are mirror polished before corrosion tests in order to obtain a smooth surface. Three samples can be held on the rotating shaft during experiments.

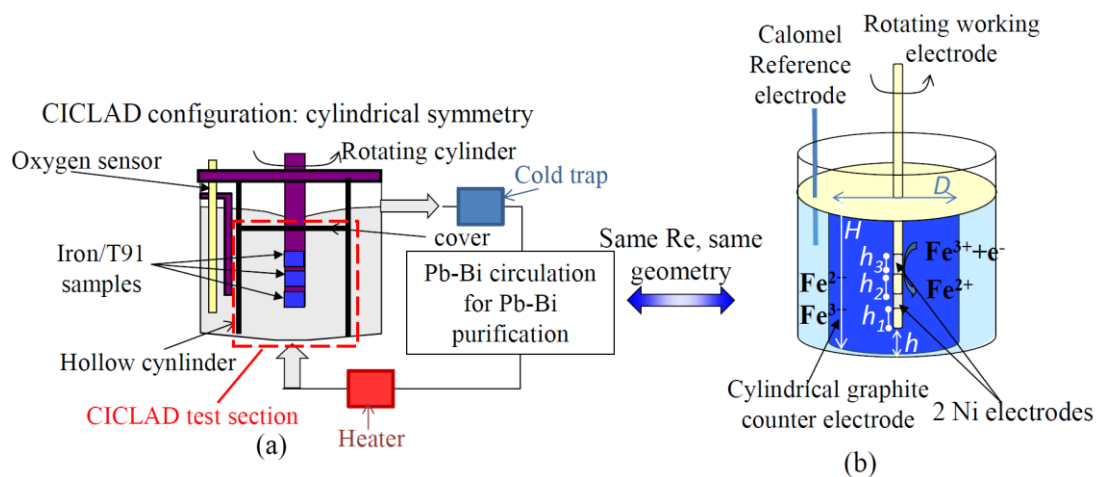


Figure 3. (a) Schematic of corrosion test section of CICLAD and (b) diagram of the electrochemical experiment.

An oxygen sensor, constituted by yttria doped zirconia [17,23,24], is immersed in LBE. It allows a continuous measurement of dissolved oxygen.

The test section has been designed to avoid perturbation of the liquid alloy flow by presence of obstacles: revolution symmetry is achieved by adding a hollow cylinder containing the rotating shaft; the oxygen sensor is thus not enclosed in the rotating LBE flow (Figure 3a). As seen on figure 3, a rigid lid has been introduced in the set-up to avoid free surface deformations. Indeed, before implementing the lid in the device, a vortex phenomenon had been observed at the liquid alloy surface and corrosion of the upper sample was much higher than corrosion of others samples [17].

To prevent dissolved iron saturation in the LBE bulk, the CICLAD facility has a LBE purification loop, including a cold trap (Figure 2). The cold trap is a part of the purification loop in which the temperature (typically 200°C) is locally lower than in the test section (between 450 and 550°C). As the solubility limit of dissolved iron in Pb-Bi increases with temperature (5×10^{-8} wt% at 200°C and 4.5×10^{-4} wt% at 550°C [25]), if the iron concentration in the Pb-Bi test section exceeds the iron solubility limit at the cold trap temperature, the excess concentration precipitates when passing through the cold trap.

2-2 Principle of the experimental determination of mass transfer coefficient in a scaled model of CICLAD

Electrochemical techniques are often used to measure mass transfer coefficient for rotating cylindrical electrodes. The methodology is for instance described by Eisenberg [20]. A scaled electrochemical ~~model~~ experiment of CICLAD is set up (Figure 3b). The scale is 1.25; ~~the~~ **this** electrochemical model is thus slightly bigger than CICLAD. Dimensions of the ~~disposal~~ **facility** are presented in Table 1.

Cell dimensions (mm) (See Figure 1)							
Cylinder diameter (mm)	Cylinder surface area (cm ²)	D	H	h	h1	h2	h3

10	7.85	122	241	116	154.5	2.5	25
----	------	-----	-----	-----	-------	-----	----

Table 1: Dimension of the electrochemical cell used to experimentally determine the mass transfer coefficient in same geometry and Reynolds number as CICLAD.

Instead of LBE, the liquid electrolyte is the one used by Eisenberg [20] : an aqueous solution composed by equimolar concentration (10^{-5} mol cm^{-3}) of $\text{Fe}^{2+}/\text{Fe}^{3+}$ added under the form $\text{K}_4[\text{Fe}(\text{CN})_6]3\text{H}_2\text{O}$ and $\text{K}_3[\text{Fe}(\text{CN})_6]$. NaOH (2×10^{-3} mol cm^{-3}) is also added to eliminate the contribution of ionic migration to mass transfer [20]. Two nickel cylinders are used as working electrodes. The counter electrode is a graphite cylinder that takes the place of the hollow cylinder in CICLAD (Figure 3). The reference electrode is the saturated calomel electrode (SCE): the redox potential of this electrode is 244.4mV versus SHE (Standard Hydrogen Electrode) at 25°C.

A potential difference is applied between the counter electrode and one of the nickel electrodes leading to reduction of ferric ions at nickel surface. The stationary current, J_{stat} , is measured at the nickel electrode interface by potentiodynamic measurements. The potential range is between 0.44 and -0.36 V/SHE and the scanning rate is 0.5 mV/s.

This steady state current, J_{stat} , is given by relation (1):

$$J_{stat} = F D_{\text{Fe}^{3+}} \frac{[\text{Fe}^{3+}]}{\delta} = FK[\text{Fe}^{3+}] \quad (1)$$

with F the Faraday's constant, $D_{\text{Fe}^{3+}}$, the ferric ion diffusion coefficient in water ($\text{cm}^2 \text{s}^{-1}$), $[\text{Fe}^{3+}]$, the ferric ion concentration in the solution equal to 10^{-5} mol cm^{-3} , δ (cm), the diffusion boundary layer thickness and K (cm s^{-1}), the mass transfer coefficient. The mass transfer coefficient, or equivalently the diffusion boundary layer, δ , can thus be deduced from relation (1) and be investigated as a function of the angular velocity of the cylinder.

Let us recall that experimental results from a scaled model are quantitatively representative of the modelled reality (here CICLAD) if at least all dimensionless parameters but one have the same value in the model as in reality. In the present problem the relevant dimensionless parameters are clearly the Reynolds number Re , characterizing the intensity of the fluid flow and its turbulence, the Schmidt number, Sc , characterizing the dissolve species ability to diffuse within the liquid, and the Sherwood number, Sh ,

quantifying the mass transfer at the liquid/solid interface. In the present work, they respectively have the following expressions:

$$Re = \frac{\omega d^2}{\nu}, Sc = \frac{\nu}{D}, \text{ and } Sh = \frac{Kd}{D}.$$

The ferric ions diffusion coefficient has been previously measured, according to Levich theory, using a rotating disc electrode: the obtained diffusion coefficient of ferric ion in this solution is $4.5 \times 10^{-10} \text{ m}^2 \text{ s}^{-1}$ [20]. The electrode diameter, d , is of 0.01m. The rotating electrode velocity can be adjusted between 10 and 733 rad s^{-1} so that the corresponding Reynolds numbers is between 5×10^2 and 3.6×10^4 .

In the CICLAD device, the samples diameter is $8 \times 10^{-3} \text{ m}$ and the rotating velocity can be adjusted between 40 and 500 rad s^{-1} . The Reynolds number varies then between 10^4 and 1.3×10^5 as the Pb-Bi kinematic viscosity is equal to $\nu (\text{m}^2 \text{ s}^{-1}) = \frac{\eta (\text{Pa s})}{\rho (\text{kg m}^{-3})}$ with the dynamic viscosity $\eta (\text{Pa s}) = 4.94 \cdot 10^{-4} \text{Exp} \left(\frac{754.1}{T} \right)$ and the density $\rho (\text{kg m}^{-3}) = 11065 - 1.293T$ [16]. Physicochemical data used to compute the parameters are gathered together in Table 2.

Iron solubility limit in LBE	$S_{Fe} (\text{mol.m}^{-3})$	$18.27 \text{Exp} \left(-\frac{10085.3}{T} \right) (11065 - 1.293T)$
Iron diffusion coefficient in pure lead	$D_{Fe}^{Pb} (\text{m}^2 \text{s}^{-1})$	$4.898 \cdot 10^{-7} \text{Exp} \left(-\frac{43934.77}{RT} \right)$
LBE kinematic viscosity	$\nu (\text{m}^2 \text{s}^{-1})$	$\frac{4.94 \cdot 10^{-4}}{11065 - 1.293T} \text{Exp} \left(\frac{754.1}{T} \right)$
Ferric ion concentration in water	$[\text{Fe}^{3+}] (\text{mol.m}^{-3})$	10^{-5}
Ferric ion diffusion coefficient in water*	$D_{Fe^{3+}} (\text{m}^2 \text{s}^{-1})$	$4.5 \cdot 10^{-10}$
Water kinematic viscosity*	$\nu_{water} (\text{m}^2 \text{s}^{-1})$	10^{-6}

Table 2: Parameters needed for modelling the flow in CICLAD device and in the electrochemical cell (use Kelvin for Temperature units).

* values are given for ambient temperature (at which tests were performed).

Unfortunately, the range of Reynolds number reached in the electrochemical experiment could not be as high as for the CICLAD facility due to limitations of the motor. However, the ranges in both experiments overlap for Reynolds numbers between $Re = 10^4$ and $Re = 3.6 \cdot 10^4$. The flow in this geometry is modelled by CFD using Fluent. It can reasonably be considered that if the numerical model is validated by

comparison with the electrochemical experiment until $Re = 3.6 \cdot 10^4$; it is also valid between $Re = 3.6 \cdot 10^4$ and $Re = 1.3 \cdot 10^5$ for the CICLAD facility.

2-3 Principle of the numerical determination of mass transfer coefficient in CICLAD device

To obtain the mass transfer coefficient, K , the thickness of the diffusion boundary layer is calculated. This calculation is done using a finite volume method with the fluid mechanics software Fluent, and the meshing software GAMBIT. As the CICLAD test section presents symmetry of revolution, calculation is made in two dimensions (Figure 4), using a 2D axisymmetric solver considering the swirling flow.

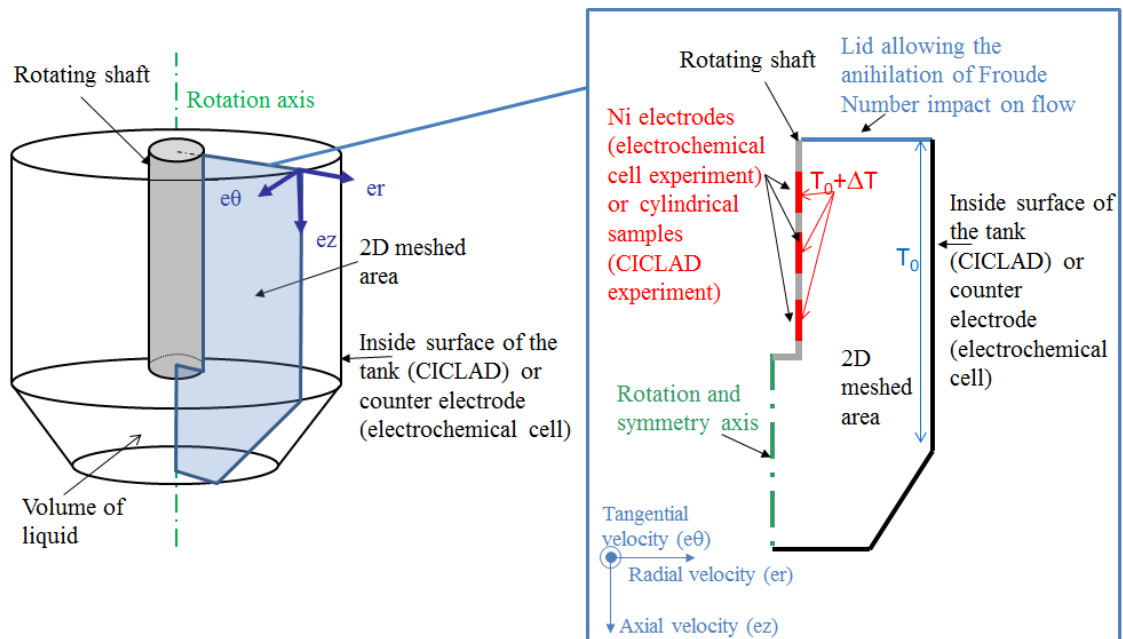


Figure 4. Diagram of the geometry considered for Fluent calculations and corresponding to both CICLAD and the electrochemical experiment geometries. On the left: a 3D representation, on the right: the used 2D domain and boundary conditions in the numerical model. Note that the rotating shaft does not reach the bottom of the tank.

The 2D meshed area of the calculation is presented on Figure 4. The minimal size of the meshing (at the rotating shaft interface) is $38 \mu\text{m}$ for angular velocities lower than 105 rad s^{-1} and 9 to $1.5 \mu\text{m}$ for higher angular velocities. This size has been computed to have several mesh cells in the chemical boundary layer, which is far thinner than the hydrodynamic boundary layer due to the high value of the Schmidt number. The used mesh has then 66 000 elements. Two coarser meshes have also been tested with the aim of assessing the validity of this mesh: the difference in computed wall shear-stresses compared to this 66000

elements mesh at the location of the electrodes/gages was 0.02% using a 41500 elements mesh and less than 2% using a 26000 elements mesh. We thus considered that the 66 000 chosen mesh was convenient and the following results were all obtained using this mesh.

The boundary conditions are the following : the lateral walls (in black on the right hand side of Figure 4) and the cover wall (in light blue) are set as fixed walls, the rotating shaft walls (in grey and red) are set as rotating walls with the nominal angular velocity, the domain is closed by a rotation axis (in green). Choice of segregated numerical solver is done as coupled solver presented some divergence issues. Pressure is discretized with “PRESTO!” scheme, as flow is mainly tangential and rotation velocity is high. Other physical quantities are discretized with a “Second Order Upwind” scheme to have better accuracy in the results. “SIMPLEX” algorithm is chosen for solving the pressure-velocity coupling in the segregated solver.

Convergence of the numerical algorithm is monitored by plotting residuals (*i.e.* estimates of the local error): this is a very classical approach in which one considers the convergence to be achieved when the plotted residuals show a decrease of several orders of magnitude and a stabilized behaviour. In addition to these very usual criteria, we have also considered that the computed shear stress on the working electrode had to have reached a steady state.

Various turbulence models have been tested leading to choose the “Reynolds Stress Model” (RSM) which modelling approach originates from Launder *et al.* [22]. This turbulence model is computationally time consuming but has been found to be necessary to reproduce the physics of this swirling flow. Indeed, an empirical criterion for choosing between this anisotropic approach and lighter isotropic turbulence model is based on the following indicator denoted *swirl number* and comparing angular momentum to axial momentum averaged on a section of the computational domain [26]:

$$S = \frac{\int r w \vec{v} \cdot d\vec{A}}{R \int u \vec{v} \cdot d\vec{A}},$$

where r is the radial position, u , v and w are respectively the axial, radial and azimuthal components of velocity and R the hydraulic diameter of the considered section.

An empirical rule of thumb is to consider that the RSM is more appropriate if S exceeds the value of 0.5 [26]. In the present case, S has been estimated from our computations to vary in the range 0.45 to 1.4 so that the RSM turbulence model was expected to be the more convenient. However, several lighter turbulence models have been tested with the objective to check if a better compromise between computational time and catching the physics of the flow was possible [27]. Figure 5 shows radial profiles

of velocity extracted from numerical simulations with 4 different turbulence models compared to measurements by 2-components Laser Doppler Anemometry in the scaled experiment presented in section 2.2. These simulations and the experimental test have been made for a rotation rate of 800 rpm and at 47.5 mm below the lid of the apparatus. Unfortunately, optical reflections and diffraction made measurements impossible near the rotating shaft and near the outer wall of the facility. One can see that the simulations using the RSM model is in good agreement with the experimental data; in particular, it adequately reproduces the azimuthal velocity profile on the contrary to the 3 other turbulence models.

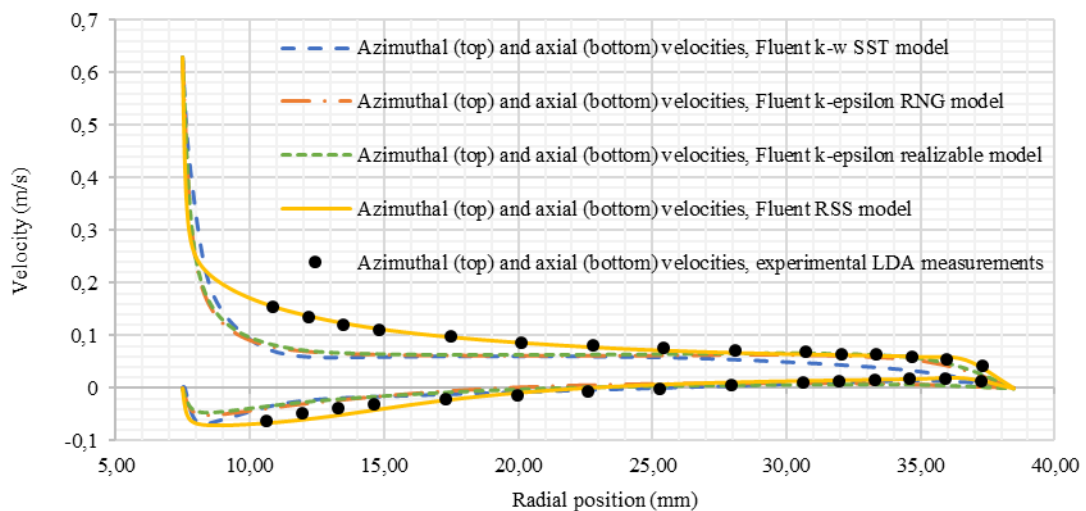


Figure 5. Radial profiles of velocity 47.5 mm below the lid of the scaled apparatus for rotation rate of 800 rpm presented in section 2.2. The measurement (dots) have been obtained with a 2-component LDA system. Four different turbulence models have been successively used to obtain the profiles plotted with lines. The profiles in the upper part of the figure are those of azimuthal velocity, the one in the lower part are profiles of axial velocities.

As a conclusion, considering the choice of the turbulence model in the simulations, the calculated flow significantly depends on the chosen turbulence model. In this rotating and confined configuration, the heavy but precise RSM turbulence model is not only adequate but also required. It has been selected for all the results presented below.

The determination of the mass transfer coefficient requires the calculation of the concentration field in the liquid near the samples/liquid interface. The boundary conditions for the concentration field are imposed

i.e. constant concentration at the working electrode surface and at the graphite counter-electrode, and impermeability, *i.e.* no flux condition, on all other surfaces (rotating shaft, cover and lower part of the inside surface of the tank). This imposed constant concentration conditions at the electrodes surfaces correspond to the case in which the anodic and cathodic reactions are limited by species diffusion. A uniform concentration in the solution is assumed as an initial condition and we compute the steady state solution of the problem. The averaged mass flux J on the working electrode is then extracted from the simulation result:

$$J = \int_S \frac{\partial c}{\partial r} dS,$$

with S the electrode surface. The mass transfer coefficient, K , is then computed from this data, knowing the dissolve specie diffusion coefficient, D , bulk concentration, c_{bulk} , and the imposed concentration at the electrode, c_i :

$$K = D \frac{J}{c_i - c_{\text{bulk}}}.$$

This mass transfer coefficient can also be expressed in its dimensionless form as the Sherwood number, Sh :

$$Sh = \frac{Kd}{D},$$

In the following, the variations of the Sherwood number will be investigated as a function of $Re^2 Sc$, with Re and Sc , the Reynolds and Schmidt numbers formerly defined. Direct correlations between dimensionless numbers are indeed expected to have the following form [20,21]:

$$Sh = a(Re^2 Sc)^b$$

with a and b two parameters to be investigated in the following.

For CICLAD experiments the concentration of dissolved elements is maintained by the Pb-Bi circulation loop with a very low flow rate (in order to avoid any modification of the flow) and its cold trap at 200°C. Consequently, in CICLAD experiments, the inside surface of the tank is inert whereas it is a counter electrode in the electrochemical experiment (Figure 3b). The boundary conditions implemented in Fluent are thus closer to those of the electrochemical experiment: when the reduction reaction occurs at the rotating working electrode producing Fe^{2+} , oxidation reaction occurs at the counter graphite electrode, consuming Fe^{2+} . These reactions lead to generate a Fe^{2+} ion flux from the working electrode to the counter electrode and the global Fe^{2+} concentration is constant. In the CICLAD experiment the iron produced by

the samples corrosion is also removed in the cold trap leading to a constant iron concentration. We consider it is reasonable to assume, in both cases, that the way the excess concentration is removed from the liquid bulk does not influence the mass transfer coefficient at the rotating shaft / electrode wall.

3 Results and discussion

Figure 6 shows the velocity field obtained with Fluent for the CICLAD experiment at 470°C for an angular velocity equal to 420 rad s⁻¹. The velocity magnitude (Figure 6a) and the tangential velocity component magnitude (Figure 6b) are plotted on the same scale showing that the tangential velocity represents the main component of the global flow. Maximum radial and axial velocities magnitudes are respectively 7 times and 26 times lower than maximum tangential velocity magnitude (Figure 6c and Figure 6d). The flow in the plane represented in Figure 6, (*i.e.* removing the tangential velocity component) is thus clearly a secondary flow. It is generated by centrifugal forces and interactions with the walls, in particular the top lid, through Eckmann type pumping: the centrifugal forces on the fluid are balanced by an outward radial pressure gradient (low pressure level near the shaft, high pressure level near the outer cylinder wall). The pressure gradient drives a radial flow near the lid (red, yellow and green zone in Figure 6.c. near the lid), due to mass conservation, this secondary flow goes down along the outer wall (red zone in Figure 6.d) thus creating a recirculation zone with minor effects on the mass transfer coefficient at the rotating shaft walls.

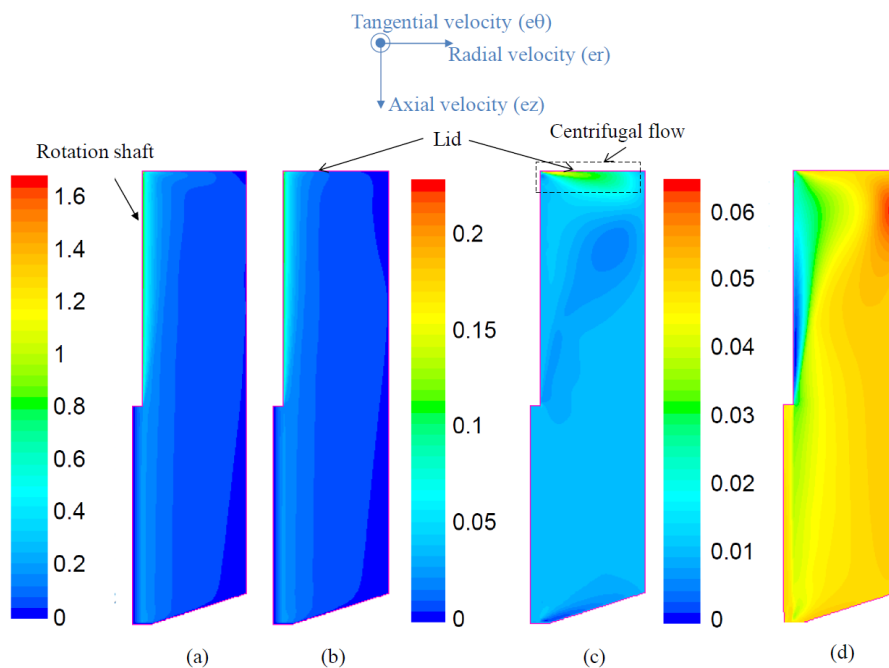


Figure 6. Numerically obtained velocity field in the CICLAD facility with Pb-Bi at 470°C and a rotating velocity equal to 420 rad s⁻¹. (a) Contours of velocity magnitude (m s⁻¹); (b) Contours of tangential velocity magnitude (m s⁻¹) same scale as (a); (c) Contours of radial velocity magnitude (m s⁻¹); (d) Contours of axial velocity magnitude (m s⁻¹).

Numerically obtained Sherwood numbers are presented on

Figure 7 as a function of Re^2Sc both for the electrochemical experiment case and for the CICLAD case with Pb-Bi at 470°C. They are compared to experimental data obtained in our electrochemical apparatus, but also to former experimental data in similar configurations [20,21]. Bars on the numerical data illustrate the size of a +/-10% interval around these predictions.

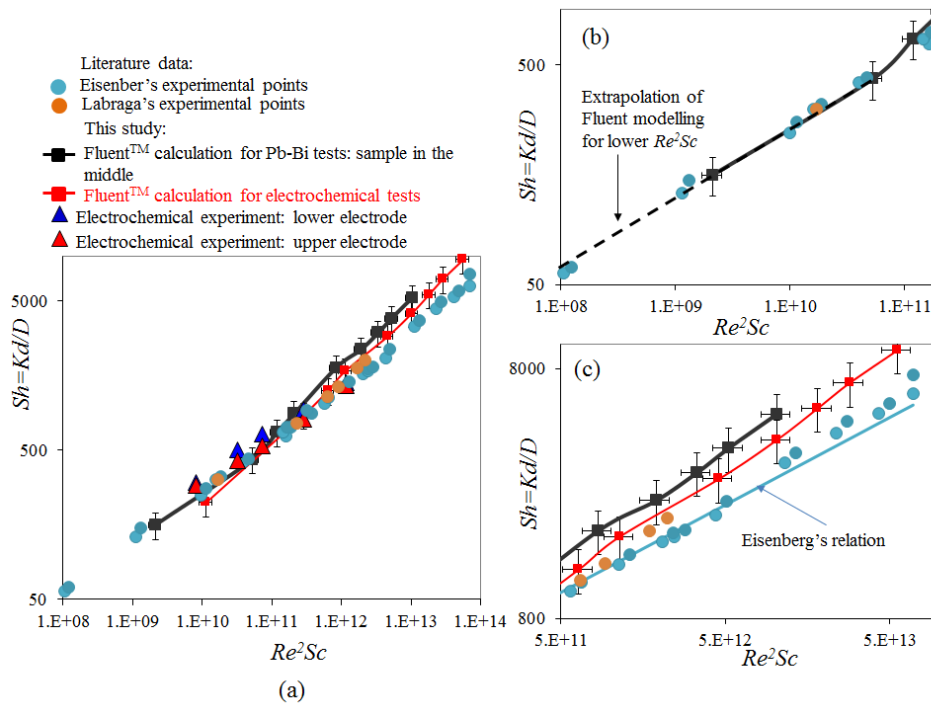


Figure 7. Sherwood number $Sh = \frac{Kd}{D}$ as a function of Re^2Sc for (a) electrochemical experiments and Fluent calculations performed for water at 25°C and Pb-Bi in CICLAD facility at 470°C (only the calculation for the sample in the middle is represented here) and comparison with Eisenberg's and Labraga's experimental data [20,21]; (b) zoom on graph (a) for low Re^2Sc for CICLAD Fluent calculations and Eisenberg's and Labraga's experimental data. (c) zoom on graph (a) for high Re^2Sc for CICLAD and

electrochemical Fluent calculations and Eisenberg's and Labraga's experimental data. The bars on the numerical data are here to illustrate the size of a +/-10% interval around these predictions.

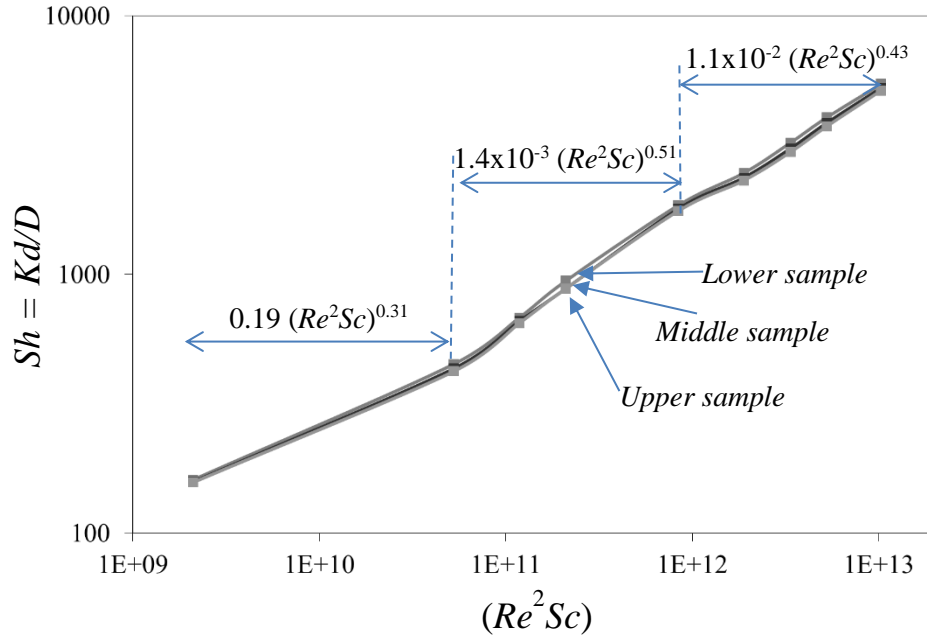


Figure 8. Sherwood number $Sh = \frac{Kd}{D}$ as a function of Re^2Sc for Fluent calculations performed for Pb-Bi in CICLAD facility at 470°C: calculations are represented here for the three samples.

As expected from the literature [20,21], our experimental measurements (

Figure 7) clearly exhibit a linear behavior in this log-log plot: $Log_{10}(Sh) = bLog_{10}(Re^2Sc) + Log_{10}(a)$ or $Sh = a(Re^2Sc)^b$. The slope, b , and the multiplicative factor, a , take slightly different values between the two electrodes and are given below (see equations (2) and (3)). Our experimental data obtained on the upper electrode are consistent with the experimental points obtained by Eisenberg and Labraga and from the Fluent calculation; the Sherwood numbers obtained with the lower electrode are between 0 and 15% higher.

Figure 7a shows that the variation of the Sherwood number with Re^2Sc , obtained by the electrochemical measurement is:

$$Sh=0.25(Re^2Sc)^{0.31} \text{ for the upper electrode;} \quad (2)$$

$$Sh=0.29(Re^2Sc)^{0.31} \text{ for the lower electrode;} \quad (3)$$

The main difference between the electrochemical measurements from this study and that of Eisenberg *et al* is that the Eisenberg's one consists of a working electrode as long as the counter electrode. On the contrary, in this study, the working electrode is shorter than the counter electrode (Figure 3b). However, the consistency between the two Eisenberg's curve and our experimental data-points in Figure 7a shows that the flow is not much affected by the cylinder length decrease.

As shown on

Figure 7a, experimental data, from this study and from literature are very close to those observed in Fluent simulations. These simulations lead to the relations:

$$Sh = 1.2 \cdot 10^{-2} (Re^2Sc)^{0.43} \quad \text{for } 10^{10} < Re^2Sc < 6 \times 10^{11} \quad (4)$$

$$Sh = 6.8 \cdot 10^{-3} (Re^2Sc)^{0.45} \quad \text{for } 10^{12} < Re^2Sc < 6 \times 10^{13} \quad (5)$$

One can notice that two trends are obtained by simulations depending on the values of Re^2Sc .

The first trend (equation (4)) covers the lower experimental Re^2Sc values, the second trend (equation (5)) is obtained for higher Re^2Sc values (i.e. higher angular velocities, and thus higher Re values). Clearly, a change in slope is observed in the vicinity of $Re^2Sc = 6 \cdot 10^{11}$: the increase in Sherwood number with Re^2Sc is slightly steeper at high Reynolds number. The relative discrepancy between relations (4) and (2 or 3) on the calculated Sherwood number is between 37% (for Re^2Sc equal to $8.02 \cdot 10^9$) and 3% (for Re^2Sc equal to $2.89 \cdot 10^{11}$).

We can conclude that the numerical model used in these Fluent simulations is validated by comparison with the electrochemical facility. Moreover, CICLAD experiments with Pb-Bi at 470°C are not only performed for higher Re^2Sc than experiments performed in the electrochemical cell but also for a slightly smaller Schmidt number, Sc ; additional CFD simulation were thus done in CICLAD conditions.

Results from numerical simulations of CICLAD experiments are plotted on

Figure 7 and Figure 8. It can be seen that the three samples located at different positions along the rotating rod have the same Sherwood number which depends on Re^2Sc according to the following laws:

$$Sh=1.9 \cdot 10^{-1}(Re^2Sc)^{0.31} \text{ or } K = 1.9 \cdot 10^{-1} \left(\frac{\omega^2 d^4}{4\nu D_{Fe}} \right)^{0.31} \frac{D_{Fe}}{d} \text{ for } 2 \cdot 10^9 < Re^2Sc < 5.3 \cdot 10^{10}; \quad (6)$$

$$Sh=1.4 \cdot 10^{-3}(Re^2Sc)^{0.51} \text{ or } K = 1.4 \cdot 10^{-3} \left(\frac{\omega^2 d^4}{4\nu D_{Fe}} \right)^{0.51} \frac{D_{Fe}}{d} \text{ for } 5.3 \cdot 10^{10} < Re^2Sc < 8.5 \cdot 10^{11}; \quad (7)$$

$$\text{and } Sh=1.1 \cdot 10^{-2}(Re^2Sc)^{0.43} \text{ or } K = 1.1 \cdot 10^{-2} \left(\frac{\omega^2 d^4}{4\nu D_{Fe}} \right)^{0.43} \frac{D_{Fe}}{d} \text{ for } 8.5 \cdot 10^{11} < Re^2Sc < 10^{13}. \quad (8)$$

with D_{Fe} : iron diffusion coefficient in LBE, ν : kinematic viscosity, d : diameter of cylindrical samples; ω : angular velocity.

Figure 7b shows that the three curves corresponding to the three samples in CICLAD geometry are superimposed. This means that same mass transfer coefficient is calculated for the three samples and then that the three samples are submitted to the same hydrodynamic flow. This feature is due to the lid presence (see Figure 3 and Figure 4). Indeed, before implementing the lid in the device, a vortex phenomenon had been observed at the liquid alloy surface and corrosion of the upper sample was much higher than corrosion of others samples [17]. The installation of the lid in the experiment allowed the suppression of the vortex and thus the decrease of the corrosion measurements discrepancies between the three samples.

Differences between the three trends (6), (7), (8), obtained for three domains of Re^2Sc consolidate the choice of using CFD calculation for determination of mass transfer coefficient. Indeed, these values of Re^2Sc could not be reached by electrochemical experiments in aqueous solution. Here again a change to a higher slope is observed at higher Re^2Sc . The change of slope is however not observed for the same value of Re^2Sc . A careful look at experimental data from the literature reinforce this observation. Indeed,

Labraga's data, plotted as orange disks in

Figure 7, clearly exhibits a similar change in slope in the high Re^2Sc range. Things are less clear

concerning Eisenberg experimental data plotted as blue disks in

Figure 7 due to some experimental dispersion, but one can consider the data cloud for abscissa between $5 \cdot 10^{12}$ and $5 \cdot 10^{13}$ to be consistent with a steeper trend too. The thorough investigation of this change of slope and its dependence on Schmidt number is out of scope of the present paper. However, it can safely be stated that this corresponds to a change from a regime in which the concentration (also called solutal) boundary layer is thinner than the hydrodynamic viscous sublayer to a regime in which they have nearly the same dimensions or even in which the viscous sublayer gets thinner than the solutal boundary layer. This regime change occurs since the thickness of these two layers does not decrease at the same rate and is sensitive to

turbulent transport within the hydrodynamic boundary layer, and thus to the Schmidt number. Note that this phenomenon has recently been observed, more deeply analysed and analytically modelled in the similar context of convection assisted dopant transport at the solid-liquid interface of solidifying silicon [28,29].

To conclude on this determination of mass transfer coefficient, electrochemical experiments allowed the validation of the Fluent simulations performed for an aqueous solution at 25°C. Once validated, this simulation has been adapted to calculate the mass transfer coefficient in Pb-Bi at 470°C, featuring a different Schmidt number. It will be considered, in our corrosion tests that the mass transfer coefficients at temperatures from 450 to 540°C are similar to the one calculated at 470°C. This mass transfer coefficient has then been used to model corrosion rate in Pb-Bi [1].

CONCLUSION

The objective of this study was to determine the mass transfer coefficient, K , on the rotating samples of the CICLAD facility. The CICLAD geometry is based on a finite rotating cylinder in a tank. The mass transfer coefficient, K , is indeed required to model the corrosion rate of steel samples fixed on a rotating shaft and dissolving into liquid Pb-Bi alloy. A scaled experimental model of CICLAD is used to validate the numerical model both concerning hydrodynamics and mass transfer. CFD calculations are performed with the Fluent software. The ability of this numerical model to reproduce the hydrodynamic flow has firstly been checked by comparison with velocity measurements in water in the scaled model. The numerical model also provides calculations of K for aqueous solutions in the interval of $Re^2Sc \in [10^{10}; 6 \cdot 10^{13}]$. These calculations are compared to experimental measurements of K performed by an electrochemical method in the same scaled model. Good agreement between experiments in aqueous solution and CFD simulation allowed the validation of the models (mesh, turbulence model, chosen solver...) used in Fluent concerning mass transfer predictions.

The same simulation was then performed for liquid Pb-Bi at 470°C and higher values of Re^2Sc . The results of the simulation show that:

- (i) The three steel samples located along the rotating shaft length undergo the same mass transfer coefficient. This suggests that corrosion of the three samples should be similar.
- (ii) In this study 3 intervals of variation of the mass transfer coefficient as function of Re^2Sc were observed:

$$Sh=1.9 \cdot 10^{-1}(Re^2Sc)^{0.31} \text{ or } K = 1.9 \cdot 10^{-1} \left(\frac{\omega^2 d^4}{4\nu D_{Fe}} \right)^{0.31} \frac{D_{Fe}}{d} \text{ for } 2 \cdot 10^9 < Re^2Sc < 5.3 \cdot 10^{10}; \quad (6)$$

$$Sh=1.4 \cdot 10^{-3}(Re^2Sc)^{0.51} \text{ or } K = 1.4 \cdot 10^{-3} \left(\frac{\omega^2 d^4}{4\nu D_{Fe}} \right)^{0.51} \frac{D_{Fe}}{d} \text{ for } 5.3 \cdot 10^{10} < Re^2Sc < 8.5 \cdot 10^{11}; \quad (7)$$

$$\text{and } Sh=1.1 \cdot 10^{-2}(Re^2Sc)^{0.43} \text{ or } K = 1.1 \cdot 10^{-2} \left(\frac{\omega^2 d^4}{4\nu D_{Fe}} \right)^{0.43} \frac{D_{Fe}}{d} \text{ for } 8.5 \cdot 10^{11} < Re^2Sc < 10^{13}. \quad (8)$$

Consequently, one can assume that the mass transfer coefficient has to be calculated in the experiment interval velocities and cannot be extrapolated from lower or higher velocities. As noticed here-above, Equation (6) corresponds to the expected Eisenberg case. The observed sensitivity of the mass transfer to the geometry is worth to be recalled. At higher Re^2Sc however, as the concentration boundary layer thickness decreases more slowly than the hydrodynamic viscous sublayer, the increase of Sherwood with Re^2Sc becomes steeper when these two thicknesses become comparable. Care must be taken that this change of slope occurs for parameters values depending on the considered species diffusion coefficient through the Schmidt number value.

Acknowledgment:

Authors want to acknowledge EUROTRANS/DEMETRA European project for its financial support together with CEA R4G project. They also acknowledge several Master students who successively worked on this subject at INSA Lyon: B. D'Aure, A. Bessette, N. Baumet, Marillier and R. Tailler.

References

- [1] L. Martinelli, K. Ginestar, V. Botton, C. Delisle, F. Balbaud-Célérier, Corrosion of T91 and pure iron in flowing and static Pb-Bi alloy between 450 °C and 540 °C: experiments, modelling and mechanism, *Corrosion Science*. 176 (2020) 108897. <https://doi.org/10.1016/j.corsci.2020.108897>.
- [2] L. Martinelli, C. Jean-Louis, B.-C. Fanny, Oxidation of steels in liquid lead bismuth: Oxygen control to achieve efficient corrosion protection, *Nuclear Engineering and Design*. 241 (2011) 1288–1294.
- [3] J. Liu, Q. Shi, H. Luan, W. Yan, W. Sha, W. Wang, Y. Shan, K. Yang, Lead–Bismuth Eutectic Corrosion Behaviors of Ferritic/Martensitic Steels in Low Oxygen Concentration Environment, *Oxidation of Metals*. 84 (2015) 383–395.
- [4] F.J. Martín-Muñoz, L. Soler-Crespo, D. Gómez-Briceño, Corrosion behaviour of martensitic and austenitic steels in flowing lead–bismuth eutectic, *Journal of Nuclear Materials*. 416 (2011) 87–93.
- [5] Y. Dai, W. Gao, T. Zhang, E. Platacis, S. Heinitz, K. Thomsen, A comparative study on the compatibility of liquid lead–gold eutectic and liquid lead–bismuth eutectic with T91 and SS 316LN steels, *Journal of Nuclear Materials*. 431 (2012) 113–119.
- [6] A. Doubková, F. Di Gabriele, P. Brabec, E. Keilová, Corrosion behavior of steels in flowing lead–bismuth under abnormal conditions, *Journal of Nuclear Materials*. 376 (2008) 260–264.
- [7] F. Gnecco, E. Ricci, C. Bottino, A. Passerone, Corrosion behaviour of steels in lead–bismuth at 823 K, *Journal of Nuclear Materials*. 335 (2004) 185–188.

- [8] I.V. Gorynin, G.P. Karzov, V.G. Markov, V.A. Yakovlev, Structural materials for atomic reactors with liquid metal heat-transfer agents in the form of lead or lead–Bismuth alloy, *Metal Science and Heat Treatment*. 41 (1999) 384–388.
- [9] Y. Kurata, Corrosion experiments and materials developed for the Japanese HLM systems, *Journal of Nuclear Materials*. 415 (2011) 254–259.
- [10] Y. Kurata, M. Futakawa, S. Saito, Corrosion behavior of steels in liquid lead–bismuth with low oxygen concentrations, *Journal of Nuclear Materials*. 373 (2008) 164–178.
- [11] A.K. Rivai, M. Takahashi, Corrosion characteristics of materials in Pb–Bi under transient temperature conditions, *Journal of Nuclear Materials*. 398 (2010) 139–145.
- [12] D. Sapundjiev, S. Van Dyck, W. Bogaerts, Liquid metal corrosion of T91 and A316L materials in Pb–Bi eutectic at temperatures 400–600°C, *Corrosion Science*. 48 (2006) 577–594. <https://doi.org/10.1016/j.corsci.2005.04.001>.
- [13] C. Schroer, A. Skrypnik, O. Wedemeyer, J. Konys, Oxidation and dissolution of iron in flowing lead–bismuth eutectic at 450 C, *Corrosion Science*. 61 (2012) 63–71.
- [14] M.P. Short, R.G. Ballinger, H.E. Hänninen, Corrosion resistance of alloys F91 and Fe–12Cr–2Si in lead–bismuth eutectic up to 715 C, *Journal of Nuclear Materials*. 434 (2013) 259–281.
- [15] L. Martinelli, F. Balbaud-Célérier, G. Picard, G. Santarini, Oxidation mechanism of a Fe-9Cr-1Mo steel by liquid Pb–Bi eutectic alloy (Part III), *Corrosion Science*. 50 (2008) 2549–2559.
- [16] C. Fazio, V.P. Sobolev, A. Aerts, S. Gavrillov, K. Lambrinou, P. Schuurmans, A. Gessi, P. Agostini, A. Ciampichetti, L. Martinelli, Handbook on lead-bismuth eutectic alloy and lead properties, materials compatibility, thermal-hydraulics and technologies-2015 edition, Organisation for Economic Co-Operation and Development, 2015.
- [17] F. Balbaud-Célérier, A. Terlain, Influence of the Pb–Bi hydrodynamics on the corrosion of T91 martensitic steel and pure iron, *Journal of Nuclear Materials*. 335 (2004) 204–209.
- [18] F. Balbaud-Celerier, L. Martinelli, Modeling of Fe–Cr Martensitic Steels Corrosion in Liquid Lead Alloys, *Journal of Engineering for Gas Turbines and Power*. 132 (2010).
- [19] M. Kondo, M. Takahashi, T. Suzuki, K. Ishikawa, K. Hata, S. Qiu, H. Sekimoto, Metallurgical study on erosion and corrosion behaviors of steels exposed to liquid lead–bismuth flow, *Journal of Nuclear Materials*. 343 (2005) 349–359. <https://doi.org/10.1016/j.jnucmat.2004.08.037>.
- [20] M. Eisenberg, C.W. Tobias, C.R. Wilke, Ionic Mass Transfer and Concentration Polarization at Rotating Electrodes, *J. Electrochem. Soc.* 101 (1954) 306. <https://doi.org/10.1149/1.2781252>.
- [21] L. Labraga, N. Bourabaa, T. Berkah, Wall shear stress from a rotating cylinder in cross flow using the electrochemical technique, *Exp Fluids*. 33 (2002) 488–496. <https://doi.org/10.1007/s00348-002-0504-x>.
- [22] B.E. Launder, G.J. Reece, W. Rodi, Progress in the development of a Reynolds-stress turbulence closure, *Journal of Fluid Mechanics*. 68 (1975) 537–566.
- [23] J.-L. Courouau, Electrochemical oxygen sensors for on-line monitoring in lead–bismuth alloys: status of development, *Journal of Nuclear Materials*. 335 (2004) 254–259.
- [24] V. Ghetta, F. Gamaoun, J. Fouletier, M. Hénault, A. Lemoulec, Experimental setup for steel corrosion characterization in lead bath, *Journal of Nuclear Materials*. 296 (2001) 295–300.
- [25] S. Gossé, Thermodynamic assessment of solubility and activity of iron, chromium, and nickel in lead bismuth eutectic, *Journal of Nuclear Materials*. 449 (2014) 122–131.
- [26] Fluent Inc., *Fluent 6 Users Guide*, in: 2003.
- [27] R. Tailler, Influence de l’hydrodynamique sur la corrosion pour un cylindre tournant, Master Thesis, MEGA, INSA Lyon, University of Lyon, 2006.
- [28] M. Chatelain, S. Rhouzlane, V. Botton, M. Albaric, D. Henry, S. Millet, D. Pelletier, J.P. Garandet, Towards wall functions for the prediction of solute segregation in plane front directional solidification, *Journal of Crystal Growth*. 475 (2017) 55–69. <https://doi.org/10.1016/j.jcrysgro.2017.05.019>.
- [29] M. Chatelain, M. Albaric, D. Pelletier, V. Botton, Solute segregation in directional solidification: Scaling analysis of the solute boundary layer coupled with transient hydrodynamic simulations, *Journal of Crystal Growth*. 430 (2015) 138–147. <https://doi.org/10.1016/j.jcrysgro.2015.08.013>.